THE ASTROPHYSICAL JOURNAL, 441:680–688, 1995 March 10

EVIDENCE FOR ELEMENTAL VARIATION IN THE EJECTA OF THE TYCHO SUPERNOVA REMNANT

O. VANCURA, P. GORENSTEIN, AND JOHN P. HUGHES
Harvard-Smithsonian Center for Astrophysics, 60 Garden Street, Cambridge, MA 02138;
email: vancura@cfa.harvard.edu
Received 1994 June 17; accepted 1994 September 12

ABSTRACT

We present an X-ray study of the Tycho supernova remnant utilizing archival data from the high-resolution imagers (HRIs) on *Einstein* and *ROSAT*, the low-energy imaging telescopes (LEITs) on *EXOSAT*, and spectral data from the Broad Band X-ray Telescope (BBXRT). We have made use of the differing HRI bandpasses to construct images of Tycho in two spectral bands, 0.7–1.8 keV and 1.8–4.5 keV. We find that the two images differ, with the harder image showing enhanced emission along much of the south, west, and north periphery. There appears to be enhanced soft emission in the interior and in one particular knot of emission in the southeast. Besides continuum (which we model here as thermal bremsstrahlung emission), we believe the hard image shows primarily the distribution of high-ionization Si and S K-shell lines which lie in the 1.8–2.6 keV band, while the softer image has contributions from Si as well as Fe XVII to Fe XXIV L-shell lines in the 0.7–1.4 keV band. Guided by the results of nonequilibrium ionization modeling of the BBXRT spectral data, we interpret the observed contrast in hard and soft X-ray emission in terms of variations in abundance, ionization timescale, and temperature. The most likely explanation for the spectral differences are spatial variations of the relative abundances of Si, S, and Fe.

Subject headings: ISM: individual (Tycho's supernova) — shock waves — supernova remnants — X-rays: ISM

1. INTRODUCTION

One of the important observational questions regarding young, ejecta-dominated supernova remnants (SNRs) is whether their X-ray emissions exhibit spatially dependent spectral variations. To date, it has been difficult to address this question because spatial studies of young SNRs have lacked spectral information, and spectral studies have had limited spatial resolution. Herein, for the first time, we attempt to make use of differing spectral bandpasses between separate imaging instruments to produce images with both moderate spatial and spectral information.

Because the X-ray emission of young SNRs is dominated by line emission from the astrophysically abundant elements oxygen through iron, joint spatial/spectral data can be used to probe the spatial distribution of the chemical elements in the remnant. At the most basic level this allows researchers to differentiate between major constituents to the X-ray emission such as the reverse-shocked ejecta, which should show abundances consistent with explosive nucleosynthesis, and swept-up interstellar medium, which should show a more "normal" composition.

Joint spatial/spectral data can also provide information on the extent of radial clumping and/or mixing that may have occurred during and since the supernova explosion. Radial stratification of the ejecta in Type Ia supernovae, in particular between the zones of Fe and of Si plus S, is predicted in white dwarf deflagration models. This is expected to occur because the elements Ne to Ca are synthesized only in intermediate temperature zones as, due to expansion, the deflagration is extinguished (Nomoto, Thielemann, & Yokoi 1984; Branch et al. 1985; Woosley & Weaver 1986). However, the extent of mixing in the early stages is unclear, as the propagation of the convective flame may be unstable to Rayleigh-Taylor processes (Woosley, Axelrod, & Weaver 1984). At later epochs, clumping (and possible further mixing) in SN ejecta has been proposed to arise from Rayleigh-Taylor instabilities generated during the deceleration of the ejecta by the circumstellar medium and formation of the reverse shock (Gull 1973; Cowie 1975; Chevalier & Klein 1978). For many remnants (e.g., Cas A; Chevalier & Kirshner 1979), optical data can provide some information on this issue. However, there is a certain class of remnants, specifically those known as Balmer-dominated, for which the optical emission shows only lines from hydrogen (see, for example, Smith et al. 1991) and so studies of the spatial variation of composition in the optical band are not possible. Nevertheless, knowledge of the chemical inhomogeneity in young SNRs is of fundamental importance to our understanding of the formation and evolution of SNRs and should be pursued in the X-ray band.

Toward this end, we have used the *Einstein* and *ROSAT* HRI data for the remnant of SN 1572 observed by Tycho Brahe to create images in two X-ray bandpasses, 0.7–1.8 keV and 1.8–4.5 keV. These bandpasses potentially sample emission from different elements, in particular Fe L shell (~0.8–1.2 keV) and Si Kα (~1.8 keV) emission in the 0.7–1.8 keV region, and Si Kα, Si Kβ (~2.1 keV), S Kα (~2.45 keV), and S Kβ (~2.6 keV) emission in the 1.8–4.5 keV range. Differences between the two images, in conjunction with the integrated spectral information provided by spectrometers like BBXRT or *ASCA*, can be used to address abundance, ionization, and/or temperature variations.

Based on analysis of the historical light curve (Baade 1945), Tycho's SNR is believed to be the remnant of a Type Ia supernova, although agreement on this point is not universal (Doggett & Branch 1985). With an age of some 420 years, the remnant is young enough for the bulk of the emission to arise from shocked-heated SN ejecta. In the optical band, Tycho is the prototypical Balmer-dominated SNR. The SNR spans 8′ in diameter, corresponding to a linear diameter of ~6 pc assuming a distance of ~2.5 kpc (Raymond 1984).

We derive an interstellar column density along the line of sight to Tycho of ~6.8×10^{21} cm^{-2}; other estimates in the literature range from 3×10^{21} cm^{-2} (Seward, Gorenstein, & Tucker 1983) to 1.2×10^{22} cm^{-2} (Itoh, Masai, & Nomoto 1988). Such a high absorbing column density is a necessary condition for the technique we outline below to work effectively. This is because the effective area curves of the *Einstein* HRI and *ROSAT* HRI (and *EXOSAT* Low Energy Imaging Telescopes [LEIT]) differ significantly below 0.7 keV, so targets for this kind of study require sufficient intervening material ($> 5 \times 10^{21}$ cm^{-2}) to extinguish all flux below 0.7 keV.

Previously, Seward et al. (1983) have discussed the extent of the blast wave, shocked ejecta, and clumping in Tycho. Chevalier, Blondin, & Emmering (1992), in modeling the growth of ejecta instabilities, found the predicted sizes of clumps in Tycho to be comparable to the observations of Seward et al. Hamilton, Sarazin, & Szymkowiak (1986) have proposed a radially stratified ejecta model of Tycho, where the reverse shock has only recently begun to enter the Fe rich of ejecta. Hughes (1991), using line centroids of the K lines of Si and Fe, found the first direct observational evidence for such radial stratification. Petre et al. (1992), using BBXRT data, have also demonstrated that the plasma diagnostics of Tycho show disparate regions between Fe and the lighter elements.

In this paper, we display evidence for the elemental stratification of ejecta clumps within Tycho. The organization of the paper is as follows. Section 2 outlines the observations and data reduction procedures. Section 3 comprises an analysis and discussion, while § 4 is a brief summation.

2. OBSERVATIONS

2.1. *Imaging Data*

We initially surveyed imaging data from the *Einstein* HRI (Giacconi et al. 1979; Henry & Henriksen 1986), *ROSAT* HRI (Zombeck et al. 1990), and *EXOSAT* CMA (Taylor et al. 1981; de Korte et al. 1981) instruments. In Table 1 we present a log of the observations, which span more than 10 years. Integration times on Tycho were 50.4, 21.2, and 59.5 ks for *Einstein*, *ROSAT*, and *EXOSAT*, respectively. The images from each instrument were aligned and co-added. For *EXOSAT*, we also weighted each LEIT/filter combination by its appropriate integration time to obtain a composite effective area as a function of energy for the entire *EXOSAT* dataset.

Because the *Einstein* HRI has response to ~4.5 keV, while the *ROSAT* and *EXOSAT* imaging telescopes have throughput only to ~2 keV, we can potentially use spectroscopic differencing between (1) *Einstein* and *ROSAT*, or (2) *Einstein* and *EXOSAT* to produce the resultant images. In Figure 1, we present the effective area curves of *Einstein*, *ROSAT*, and *EXOSAT*, after multiplying by the X-ray opacity corresponding to an ISM column of 6.8×10^{21} cm^{-2} using the cross sections and abundance data from Morrison & McCammon (1983). For this value of N_H, almost all emission below 0.7 keV is absorbed. In Figure 2, we show the *Einstein* and *ROSAT* bandpasses with $N_H = 6.8 \times 10^{21}$ cm^{-2}, after scaling the effective area of *Einstein* by a factor of 5. Also shown is the "Difference" curve, obtained by subtracting the *ROSAT* effective area curve from that of the scaled *Einstein*.

TABLE 1

LOG OF OBSERVATIONS OF TYCHO

Satellite	Date	Time (s)
Einstein	1979 Feb 8	50409
EXOSAT	1983 Sep 25	14020
	1984 Aug 16	13993
	1984 Aug 16	31467
ROSAT	1990 Jul 28	21153

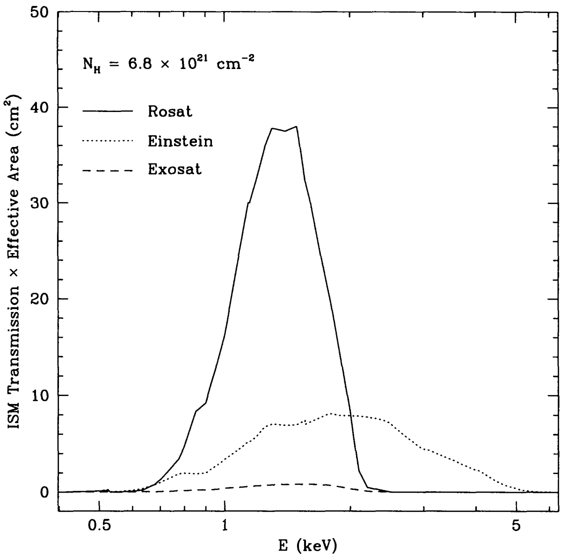

FIG. 1.—Effective area curves. The effective area curves of *Einstein*, *ROSAT*, and *EXOSAT*, allowing for transmission through a column density of 6.8×10^{21} cm^{-2}. Although it is difficult to tell from this figure, the bandpasses of *ROSAT* and *EXOSAT* are very similar.

The *ROSAT* and *EXOSAT* spectral bandpasses are very similar. For *ROSAT*, the counting rate was 7.8 counts s^{-1} for the entire source with a background rate of 1.1×10^{-2} counts arcmin^{-2} s^{-1}. For *EXOSAT*, the corresponding rates were 0.23 counts s^{-1} and 2.0×10^{-3} counts arcmin^{-2} s^{-1}, while for

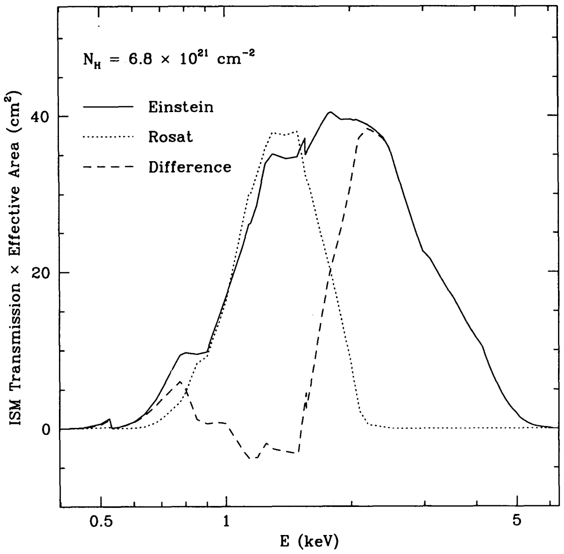

FIG. 2.—Comparison of *Einstein* and *ROSAT* effective areas. The *Einstein* curve has been scaled by a factor of 5. Also shown is the "Difference" curve. The *ROSAT* and Difference images can be used to isolate emission in the 0.7–1.8 keV and 1.8–4.5 keV bands.

Einstein the rates were 2.9 counts s^{-1} and 7.0×10^{-3} counts $arcmin^{-2}$ s^{-1}. With the integration times above, the *ROSAT* Tycho image thus has 12 times as many source counts as that of *EXOSAT*. For several regions in the remnant, including those both bright and faint, we have calculated the ratio of *ROSAT* to *EXOSAT* counting rates, finding that within statistics the *ROSAT* and *EXOSAT* images are equivalent and consistent with the hypothesis of having arisen from the same source. Because the *ROSAT* spatial response and signal-to-noise is much better than that of *EXOSAT*, we have continued our analysis using only the *ROSAT* and *Einstein* data.

A major consideration in preparation for comparing the SNR images is the correction for the different point response functions (PRFs) between the instruments. The PRF of *Einstein* is somewhat sensitive to the source spectrum because of the strong energy dependence of X-ray scattering from the mirror surface. As such, we attempted to determine an appropriate PRF for *Einstein* by comparison with a source spectrally similar to the SNR. In so doing, we have adopted model fits to Cygnus X-1 data. For *ROSAT*, we have adopted the nominal PRF (Zombeck et al. 1990), since the PRF is not a sensitive function of energy. The published analytic expression for the *Einstein* HRI PRF (Henry & Henriksen 1986) is based on Cygnus X-2, which has a softer spectrum than Tycho. Although our derived *Einstein* PRF is broader than that given in the literature, our results are fairly robust with respect to the exact choice of PRF. In Figure 3 we present the adopted PRFs for the instruments. The 50% encircled energy radius is ~3″ for *ROSAT* and ~6″ for *Einstein*. The PRF for the *EXOSAT* data is shown as well. The broadness of this function is another reason for rejecting the *EXOSAT* data from further consideration in favor of *ROSAT*.

We expect some expansion to have occurred between the *ROSAT* and *Einstein* images since Tycho is only ~420 yr old and the data were taken ~11.5 yr apart. Without any scaling, many features in the *ROSAT* image appear to have moved radially outward from their counterparts in the *Einstein* data. In order to coalign most features well, we enlarged the *Einstein* image by 1.4% while conserving flux and resampling to maintain the same pixel sizes. This factor of 1.4% corresponds to an expansion rate of 0″.3 yr^{-1}, making the apparent X-ray expansion rate consistent with the optical filamentary proper motion of 0″.3 yr^{-1} (Kamper & van den Bergh 1978).

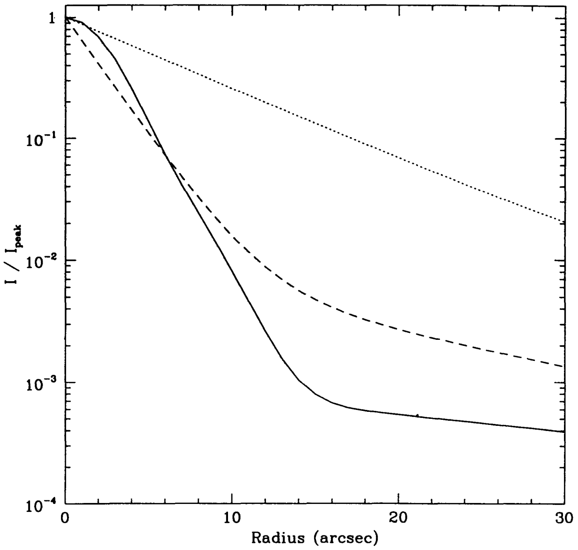

FIG. 3.—Point response functions for the different instruments. The solid, dashed, and dotted curves represent the *ROSAT* HRI, the *Einstein* HRI, and the *EXOSAT* LEITs, respectively.

To place the Tycho images on the same spatial resolution, we convolved the *ROSAT* image to the approximate imaging resolution of *Einstein* in the following manner. First, we effectively removed the *ROSAT* PSF from the *ROSAT* image using image deconvolution techniques (Lucy 1974). The deconvolution ran for three iterations and was accomplished using tasks within IRAF. We then convolved the resultant image with the PRF of *Einstein*, to produce a convolved *ROSAT* image with spatial resolution approximating that of *Einstein*. A constant background level, determined from regions free of SNR emission, was then subtracted. An intensity-dependent smoothing algorithm was applied in order to reduce statistical fluctuations while, at the same time, retaining true high-frequency image structure. To obtain a constant statistical uncertainty in each pixel in the smoothed image, we varied the standard deviation of the smoothing kernel as the inverse square root of the counts in the pixel. In actual practice, only five levels were used with standard deviations varying between 6″ and 18″. The enlarged *Einstein* image was background subtracted and adaptively smoothed with the same filters such that the same smoothing length scale was used on a pixel-by-pixel basis for the *ROSAT* and *Einstein* images. Finally, we scaled the *Einstein* smoothed image by a normalization factor (2.1) obtained by multiplying the effective area scaling factor (5) by the ratio of integration times (*ROSAT*/*Einstein* = 0.42). The resultant *ROSAT* image was subtracted from the final *Einstein* image to produce a "Difference" image, with the bandpass shown in Figure 2.

In Figure 4 (Plate 18), we show the respective *Einstein* and *ROSAT* images of Tycho. Figure 4*a* (top left panel) shows the final *Einstein* Tycho image, after background subtraction, adaptive smoothing, and normalization. Figure 4*b* (top right) shows the *ROSAT* Tycho image, after deconvolution/convolution, background subtraction, and adaptive smoothing. Figure 4*c* (bottom left) shows the Difference image. Study of Figures 4*b* and 4*c* indicates that there exist spatial regions dominated by varying degrees of 0.7–1.8 keV emission and 1.8–4.5 keV emission. To further illustrate these differences, we reproduce the final *ROSAT* image (Fig. 4*b*) in Figure 5 and delineate several regions of interest. For example, the large knot in the S (position A in Fig. 5) is more predominant in the difference image, while the southern knot in the SE (position B) is more visible in the *ROSAT* image. In contrast to the SE southern knot, the SE northern knot (position C) appears bright in both the *ROSAT* and difference images. To further assess the extent of the spectral differences, we have created a "Ratio" map, obtained by dividing the Difference image by the *ROSAT* image, presented as Figure 4*d* (bottom right). Overlaid for reference on the Ratio map are contours from the convolved *ROSAT* image, Figure 4*b*. The Ratio map, in effect, is a spectral hardness map, as regions showing enhanced 1.8–4.5 keV emission appear in red and yellow, and those showing enhanced 0.7–1.8 keV emission appear in green and blue. Regions showing harder ratios generally appear near the periphery. The harder ratio appears strong in the south, west, and north.

Because it is difficult to estimate the propagation of errors throughout our deconvolution/convolution process, we have developed alternative methods to assess the systematic uncer-

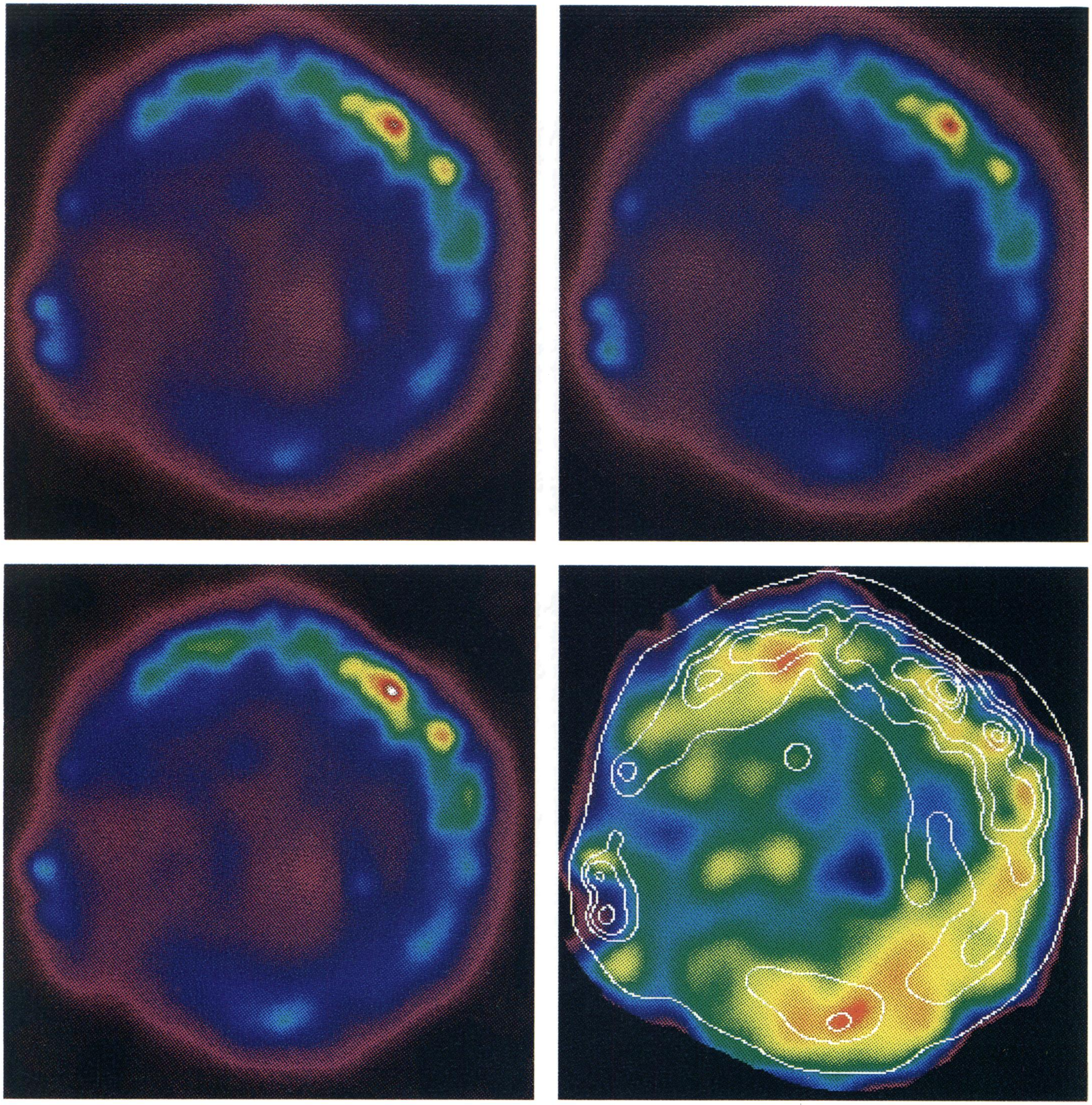

FIG. 4.—Tycho images. The four panels represent (*a*; *top left*) final *Einstein* smoothed image; (*b*; *top right*) final *ROSAT* smoothed image; (*c*; *bottom left*) Difference image; (*d*; *bottom right*) Ratio image, obtained by dividing the Difference image (*c*) by the final *ROSAT* smoothed image (*b*). Overlaid on the Ratio image are the contours from *ROSAT* (*b*). Each panel is 4'.25 by 4'.25. Low values are represented by darker colors; high values are represented by lighter colors.

VANCURA, GORENSTEIN, & HUGHES (see 441, 682)

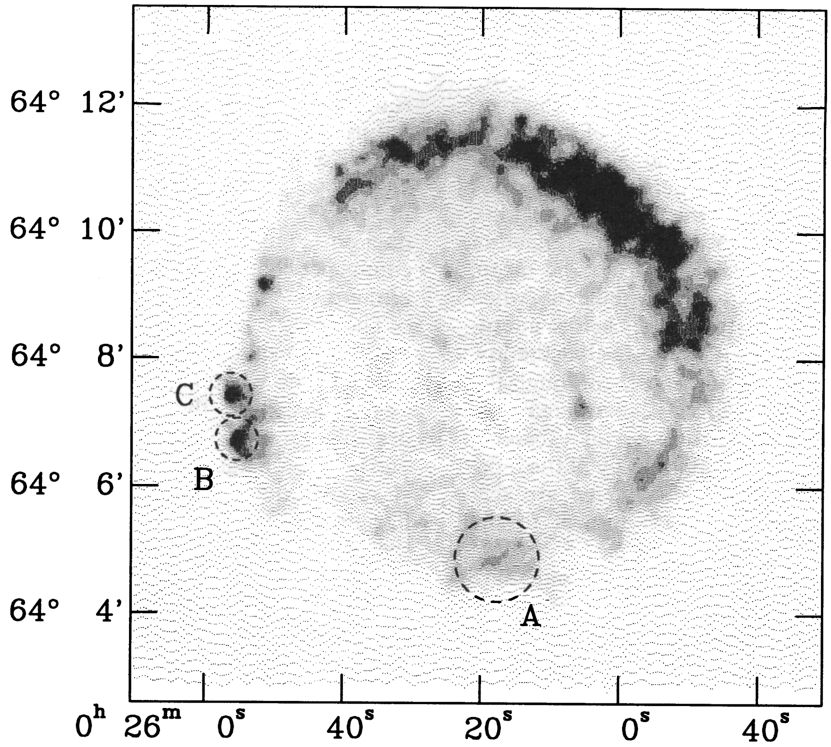

FIG. 5.—Final *ROSAT* smoothed image. This image is a reproduction of Fig. 4*b*. Overlaid are regions of interest referred to in the text.

tainties and statistical confidence in our aforementioned procedure. To address the systematic uncertainty, we have performed the following. We began with two identical copies of the deconvolved, background-subtracted *ROSAT* Tycho image. We then scaled one (to become the derived *Einstein* image) by an appropriate factor to yield the actual *Einstein* counts. Each derived image was then convolved with the appropriate PRF. Negative pixels were replaced with zeros, and an appropriate background image was added to each. At this point, the two derived images represented *Einstein* and *ROSAT* data. We then performed our reduction procedure on these two images. In the actual data, the ratio of counts from the entire SNR in the Difference and *ROSAT* bandpasses is 0.74. By construction, our derived images yield a very similar average ratio. Furthermore, deviations from this average indicate the systematic error (plus some statistical error) introduced through our analysis. The derived Ratio map appears flat for the most part, as expected. Regions appearing bright or faint in the original derived images do not appear to correlate with the final Ratio image. From the pixels comprising the derived Ratio image we find a sigma of 0.05, which (although including some statistical uncertainty) we adopt as a measure of the systematic uncertainty. To show this in a more visual way, we present a histogram of the ratio values in the actual and derived Ratio images in Figure 6. It is clear that the variation in ratio value is much greater in the actual Ratio image.

To address the statistical uncertainty for various regions in the remnant, we employed a Monte Carlo method. Assuming that the pixel values in the actual *Einstein* and *ROSAT* images were the mean, we passed each of the original images through a Poisson filter to generate randomized *Einstein* and *ROSAT* images. We then repeated the above reduction steps to produce new randomized Difference and Ratio images. In repeating this entire procedure, we developed a sample of randomized images with which to estimate statistical errors. Each of the randomized Difference (*ROSAT*) images appears substantially similar to the actual Difference (*ROSAT*) image. In particular, regions of the SNR showing enhanced or decreased emission are duplicated in the randomized images. This verifies that the features visible in the processed images, generated by our adaptive-smoothing procedure, correspond to statistically significant image structure.

For example, using a square box of side 40″ centered on the southern Ratio enhancement (A in Fig. 5) yields a ratio of counts in the Difference and *ROSAT* bandpasses of

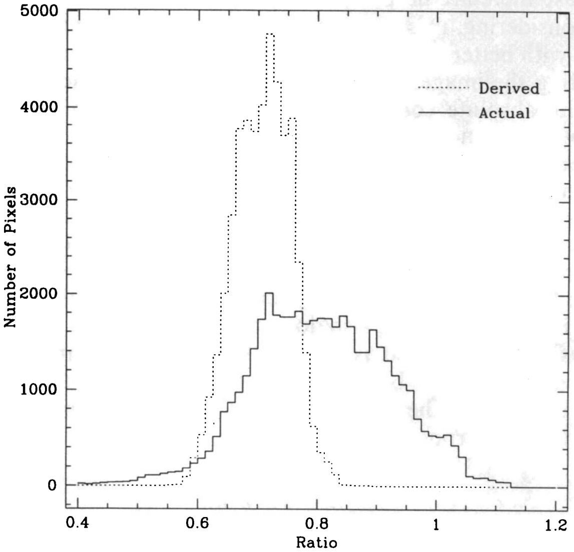

FIG. 6.—Histogram of actual and derived ratio images. Note that the total range in ratio value is much greater in the actual image. The shift toward a higher mean ratio value in the actual histogram occurs because of spatial structure affecting the nonlinear ratio function.

1.01 ± 0.03. Similarly, the NE region which appears bright in the Ratio map (Fig. 4*d*) yields a ratio of 1.10 ± 0.04. The faint region near the center of Tycho does not appear to differ significantly from the mean, with a ratio of 0.63 ± 0.07. However, the two knots of emission in the SE have ratios of (top, C in Fig. 5) 0.82 ± 0.04 and (bottom, B in Fig. 5) 0.53 ± 0.04. Adding in quadrature the systematic error derived above yields ratios of 1.01 ± 0.06 and 1.10 ± 0.07 for the S and NE regions, respectively, and 0.53 ± 0.07 for the bottom SE knot. Each of these represents a deviation of at least 3 σ from the mean. Typical enhancements also appear to be significant when counting statistics are considered for the images before adaptive smoothing is applied. (In particular, we note that the low ratio of the bottom SE knot appears to be real, although the knot is near the periphery of the remnant. Data extracted from this region in the original images also show an excess of *ROSAT* counts.) Thus, we are confident that many of the morphological features appearing in the Ratio image are real enhancements in the Difference image with respect to the *ROSAT* image.

Additional possible sources of uncertainty in our data reduction include an incorrect value for column density along the line of sight, image alignment problems, and PRF uncertainties. We address each of these in turn.

1. At any given energy, adjusting the line of sight column density will modify the transmission coefficient. However, the ratio of two effective area curves at a particular energy is independent of assumed column. Therefore, to first order, our bandpass scaling factor is independent of intervening column density provided that there is sufficient material to completely absorb X-rays less than ~0.7 keV, below which the effective areas of the different instruments diverge. Even if our assumed $N_{\rm H}$ is incorrect by a factor of 2, provided $N_{\rm H}$ is uniform, it is unlikely to negate our results (see below).

2. Image alignment is potentially troubling, but should not negate the conclusions reached above. The nominal absolute pointing accuracy for *Einstein* is ~3″ (Harris 1984), while for *ROSAT* it is ~5″–10″. Thus, relative alignment in constructing the Difference images may be in error by as much as 10″. Because there are no point sources in any of the field that we are considering, it is impossible to ascertain absolute coordinates with better than the nominal accuracy. Therefore, in constructing the images, we first aligned them using the nominal satellite absolute coordinate information. Through comparison of common features, we opted to shift the images slightly with respect to each other. However, we have tested various alignment schemes to look for variations in the resultant images. (If the images are initially misaligned by more than 4″, a telltale pattern consisting of extremely high pixels adjacent to extremely low pixels emerges on opposite sides of the remnant in the Ratio image.) We believe our alignment is good to ~2″.

3. PRF uncertainties also do not appear to negate the above analysis. We have tried assuming PRFs from softer and harder sources in order to bound what we believe to be the actual case. In all cases, the Difference and Ratio images again maintained their morphological appearance.

2.2. *Spectral Data*

We have obtained archival data on Tycho's SNR from the BBXRT X-ray mission (Serlemitsos et al. 1991) flown aboard *Astro 1* in 1990 December. Model fits were performed to the four BBXRT Tycho spectra with the greatest counting rates for the duration of the mission: A0, A2, B0, and B4. The A0 and B0 spectra were from a circular region of radius 2′ in the N and NE, while those from A2 and B4 each represent the spectra of roughly one fourth of an annulus of inner radius ~3′ and outer radius ~9′ situated in the SW. Of course, the BBXRT data sample a larger region of the remnant than is implied by the angular size of the detector pixels, because of the broad PRF of the BBXRT X-ray telescope (~3′ half-power diameter). The data energy bins were grouped so that there were at least 15 counts per channel in order that χ^2 could be used as the figure-of-merit function for determining best-fit parameters.

The spectral model we employ includes the effect of nonequilibrium ionization (NEI). Our approach avoids introducing assumptions about the dynamical evolution of SNRs by assuming instead that the emergent X-ray spectra may be described in terms of mean values for the plasma temperature and ionization age. The model represents a logical extension of such well-known and widely used collisional ionization equilibrium (CIE) models as those of Raymond & Smith (1977) to the NEI situation. An important feature of the model is the determination of the nonequilibrium ionization fractions; we use the matrix diagonalization technique developed by Hughes & Helfand (1985). Departures from ionization equilibrium are parameterized by a characteristic timescale, called the ionization age or timescale, which can be expressed dimensionally as the product of the electron density and the time since the shock passed, $n_e t$. In actual practice, interpretation of the ionization timescale derived from fits is model dependent, since the derived quantity represents an emission-weighted average over the SNR of the time integral of the electron density since the passage of the shock front. This NEI model has now been successfully applied to remnants in a number of situations (see Hughes & Singh 1994 for a recent application and more details on the model) and is available as a model in the spectral fitting package XSPEC, which we used for this analysis.

We fit the entire energy range (0.5–9 keV) to a single-temperature, single-ionization-timescale NEI plasma model, initially allowing all parameters to vary freely. These initial fits showed that the derived values for the ISM column density, kT, and $n_e t$ from the four data sets were roughly consistent with each other and so they were averaged. The values so obtained are consistent with previous determinations (Hughes 1991). The fits were redone using these average values and this time, only the abundances and an overall normalization factor were allowed to vary freely. Typically, reduced χ^2 values were ~2 for 150 d.o.f. Finally, because the pair of spectra A0 and B0 (and likewise for A2 and B4) sample much the same spatial region of Tycho, the fits were carried out with a single linked abundance set. We present the results of these final fits to the A0 + B0 and A2 + B4 data in Table 2. In Figure 7, we show the sum of all four spectra overlaid with the summed best-fit model.

The fit over the energy band of interest (0.5–4.6 keV) is generally reasonable. However, the energy band just around the Si helium-like Kα line (~1.85 keV) is not fitted well. This could be due to an instrumental effect, such as a slight energy gain shift or an effect due to the Si composition of the BBXRT detectors. The effective area of the X-ray telescope in this energy range and above may be uncertain due to the presence of the gold M-edges which tend to be rather difficult to model. Other physical effects, such as a Doppler shift could be responsible, or it may be due to a limitation in the atomic physics of our NEI code.

TABLE 2

SUMMARY OF NEI MODELING OF BBXRT TYCHO DATA

Parameter	A0 + B0	A2 + B4
$N_H(10^{21})$	6.8	6.8
kT (keV)	1.72	1.72
$\log_{10} n_e t$ (s cm^{-3})......	10.04	10.04
K[a] (10^{13} cm^{-5}).........	3.81 ± 0.22	8.32 ± 0.37
O abundance	0.18 ± 0.04	0.11 ± 0.03
Ne abundance	0.18 ± 0.04	0.12 ± 0.03
Mg abundance	0.22 ± 0.03	0.13 ± 0.02
Si abundance	5.19 ± 0.24	3.80 ± 0.15
S abundance	11.89 ± 0.81	9.11 ± 0.53
Ar abundance	2.43 ± 0.71	2.24 ± 0.52
Ca abundance	...[b]	4.21 ± 2.38
Fe abundance	0.17 ± 0.02	0.14 ± 0.02
Rate (counts s^{-1})	6.374 ± 0.06	9.426 ± 0.07

[a] $K = n_e n_i V/4\pi d^2$, where V is the volume of emitting material, and d (= 2.5 kpc) is the distance to Tycho. The emission measure ($n_e n_i V$) is $\sim 5 \times 10^{58}$ cm^{-3}.

[b] Fitted Ca abundance was 0. The error was indeterminate.

The fit above 5 keV is also not acceptable. Although it is not in our bandpass of interest, some discussion of the relevant issues seems appropriate. Our calculations indicate that the excess continuum flux observed in the data at energies above 5 keV can be reproduced if we include a power-law or very high temperature component similar to the one recently reported by Fink et al. (1994) based on *Ginga* observations. An Fe Kα line at an energy of ~6.4 keV (Petre et al. 1992) is also present. The existence of this Fe line has been known for some time (see, for example, Tsunemi et al. 1986) and has potentially important implications. The low plasma temperatures implied by the shape of the X-ray continuum emission and the observed ratios of Kα and Kβ Si and S lines, predict negligible amounts of Fe K-shell line emission. Our results, shown in Figure 7, confirm this. In their models Hamilton et al. (1986) found it necessary to mix some fraction of the Fe-rich core of ejecta out to the Si and S zone (which provided a component of Fe at a high temperature), in order to reproduce the reasonably high ratio of Fe K-shell to L-shell emission. Our preliminary calculations indicate that the observed ratio of Fe K-shell to L-shell emission can be approximately reproduced by our model if the temperature associated with the Fe emission is increased to ~10 keV. In this case the shape and intensity of the Fe L-shell emission blend around 0.8–1.2 keV changes somewhat and other parameters in the fit (principally the column density) need to be adjusted to compensate. However, it is not yet completely clear whether or not the Fe K-shell and L-shell emission come from a single component of the SNR. Our preliminary study of the Fe Kα emission suggests that the single-temperature single-timescale model presented herein is an adequate representation of the spectral data in our bandpass of interest. Further analysis and interpretation of the spectral data at energies beyond 5 keV will be the subject of future study.

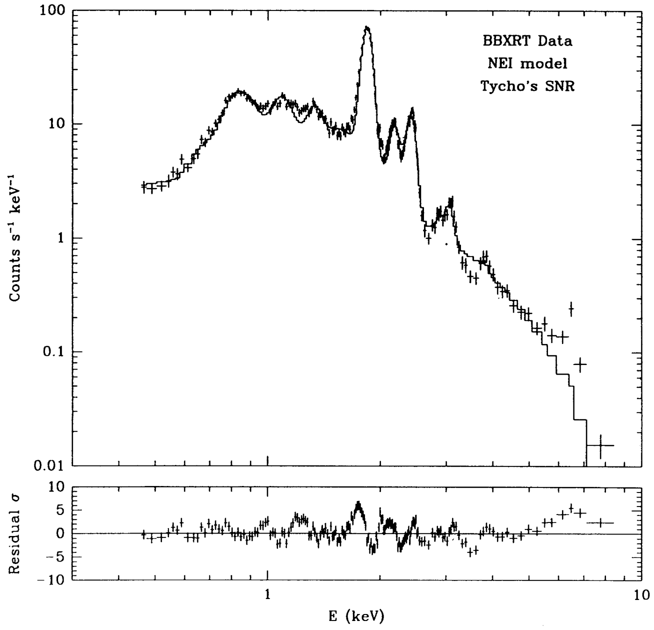

FIG. 7.—Global BBXRT data and model fit. Shown are the sum of the BBXRT data (from pixels A0, B0, A2, and B4) and the best-fit summed nonequilibrium ionization model. The residual spectrum is given in the bottom panel. Note the poor fits near the Si Kα line (~1.85 keV) and at high energies (>5 keV).

We used the results of these NEI model fits to predict values we would expect to see in our Ratio image. Model spectra were calculated based on the results from the individual fits to the four BBXRT data sets and multiplied by the respective effective area curves of the *Einstein* and *ROSAT* HRIs. The predicted ratio in the several cases fell between values of 0.77 and 0.82. Considering our systematic error, this is in excellent agreement with the actual global ratio from the imaging analysis (0.74) and the ratio averaged over the specific regions more closely corresponding to the BBXRT field of view (0.86). Furthermore, because all four BBXRT spectra, before fixing N_H, yield essentially the same ratio of counting rates between *Einstein* and *ROSAT*, our nominal choice of N_H equal to 6.8×10^{21} cm^{-2} is not crucial.

3. ANALYSIS AND DISCUSSION

We have shown that in Tycho there exist spatially distinct regions dominated by varying degrees of 0.7–1.8 keV and 1.8–4.5 keV emission. We will now discuss the origin of the emission in each band.

Previous spectral analysis of Tycho indicates that the X-ray emission is dominated by shocked ejecta. Analysis of *Einstein* SSS data by Hamilton, Sarazin, & Szymkowiak (1986) implies that the blast wave only makes a significant contribution at energies greater than 5 keV. Spectral analysis of SSS and *Tenma* data by Hughes (1991) suggests that in Tycho, the integrated emission measure due to the blast wave is only 1/20 that due to ejecta. Spectral fits to *Einstein* SSS and *Tenma* GSPC spectra (with plasma under equilibrium or nonequilibrium conditions) suggest that the *ROSAT* bandpass is dominated by a complex of 0.7–1.4 keV Fe XVII to Fe XXIV L line emission, while much of the flux between 1.8–2.6 keV is comprised of helium-like Si and S Kα and Kβ lines (Becker et al. 1979, 1980; Hamilton et al. 1986; Tsunemi et al. 1986; Jansen et al. 1988; Smith et al. 1988; Hughes 1991).

Our spectral fits to the BBXRT data suggest a similar scenario. In particular, our overall fit to the data suggests that the Difference bandpass is primarily composed of Si + S emission which accounts for 47% of the counts. Fe emission represents 16% of the counts, and "continuum" emission (consisting roughly of half due to free-free processes, and half due to lines of elements besides Fe, Si, and S) accounts for 37%. In the

ROSAT bandpass, Si (without S) and Fe emissions account for 21% and 30%, respectively, with the "continuum" accounting for 47% of the counts. With this in mind, continuum aside, the Difference image is dominated by Si + S emission, while the *ROSAT* image is dominated by high-ionization Fe and Si emission.

The Tycho Ratio image shows values ranging from ~0.55 to 1.1, with a mean of 0.74. There are several possibilities for the origin of spatially distinct regions dominated in turn by either Fe, Si, or S emissions. These include interstellar column effects, abundance effects, and plasma (temperature and ionization timescale) effects. We discuss each of these in turn.

Although Tycho is significantly far from the galactic center, making it unlikely that significant interstellar transmission variations exist across the face of the remnant, we may nevertheless ask the question whether $N_{\rm H}$ variations alone could produce the observed contrasts in the Ratio image. From the BBXRT data, we find a requisite variation in $N_{\rm H}$ of $\sim 3 \times 10^{21}$ cm^{-2} to reproduce a Ratio of 1.1. Because ratio values rise both with increasing $N_{\rm H}$ (due to the *ROSAT* bandpass transmission failling) and decreasing $N_{\rm H}$ (due to the Difference bandpass leakage at 0.8 keV becoming more predominant), we cannot reproduce a ratio below 0.7 with any reasonable change in $N_{\rm H}$. The features seen in the Ratio image have extent less than 1′, and we can assume this value for the dimension along our line of sight of any potential intervening cloud of material. At a distance of 2.5 kpc, 1′ corresponds to 0.7 pc, and to achieve a $\Delta N_{\rm H}$ of 3×10^{21} cm^{-2} requires a density in excess of 10^3 cm^{-3}. As molecular clouds possessing these densities typically span tens of parsecs, we find it extremely unlikely that variations in line of sight column depth can account for variations in the Ratio map.

We believe the most natural explanation for the structure we are seeing in the ratio map is abundance variations. Using the overall fit to the BBXRT data as our starting point, we have investigated how variations in the Fe, Si, and S abundances affect the expected ratio value. In particular, we wish to know what abundances will reproduce the range from ~0.55 to 1.1. Because we have only one constraining parameter (the ratio value), we have chosen to vary Si and S abundances simultaneously such that their relative abundance stays fixed. This is because Si and S ejecta regions are expected to be spatially correlated, in contrast to the Fe core. In Figure 8 we present the results of the abundance study. The horizontal axis represents the abundance of Si + S relative to the BBXRT mean. The vertical axis represents abundance variation for Fe. The contours represent curves with constant ratio values.

For example, a Ratio image value of 0.55 (with abundance effects alone) can be achieved in a clump of ejecta with the mean abundances of Si and S if Z(Fe) is 9 times the mean. If there is no Si and S, Z(Fe) equal to 2 times the mean reproduces a ratio of 0.55. To reproduce a ratio of 1.1, we need a factor of 4 abundance enhancement in Si + S assuming the mean abundance of Fe. If there is no Fe, the enhancement of Si + S required is a modest factor of 1.6. Thus, the required variations (to reproduce the range of observed ratios) are not enormous.

The abundance interpretation requires the ejecta to be at most only partially mixed. In particular, the data suggest enhanced Si + S near the periphery, while perhaps showing some Fe enhancement in the interior. This is consistent with ejecta models of Tycho (e.g., Hamilton et al. 1986) in which the reverse shock has perhaps only recently begun to enter the Fe-rich ejecta near the center of the expanding SNR. Furthermore, the mean abundances we derive in fitting the BBXRT data (see Table 2) are also consistent with this picture. The elements Si and S are each overabundant by factors of several over cosmic, while the Fe abundance is a fraction of the cosmic value.

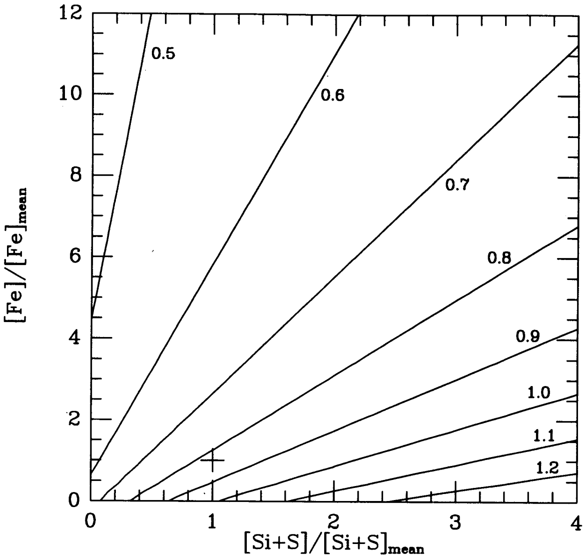

FIG. 8.—Abundance study. The contours represent constant ratio values with the mean fit denoted by a cross. Note that the entire range of the ratio image (~0.55–1.1) can be reproduced with modest (factors of several) variations in relative abundance.

As an alternate explanation, we may assume that the shocked ejecta are homogeneously mixed throughout the interior of the SNR, and that any abundance variations with position are negligible. In order to model variations observed in the Ratio map, we would then need to appeal to different temperatures and/or ionization timescales for different regions of shocked (compositionally homogeneous) ejecta. Since the reverse shock is continually encountering new ejecta material, it is possible that different temperatures and densities, (hence ionization timescales) may apply to different regions of the remnant. In particular, for Tycho-like conditions, Chevalier (1982) finds that over most of the volume of shocked ejecta, the density increases by about a factor of 2 (from larger to smaller radii), while the temperature falls by a factor of 4 over the same region.

We have used the NEI code to investigate possible plasma effects under the assumption of negligible abundance variations. We first investigated whether the observed range in our Ratio image could be reproduced keeping the ionization timescale of all the elements fixed to the mean, but allowing kT (still assumed to be the same for all elements) to vary. In Figure 9*a*, we present these results. Temperature variations can very nearly reproduce the range of ratio values we observe, however the required temperature variations span more than two orders of magnitude. This interpretation appears very unlikely in view of the models of Chevalier (1982) discussed above.

We have also investigated whether $n_e t$ effects alone can reproduce variations in our Ratio map. In Figure 9*b* we present these results. For reasonably modest variations in $n_e t$ (a factor of 3 greater than the mean), the high ratios can be reproduced, but it appears very unlikely that $n_e t$ effects alone

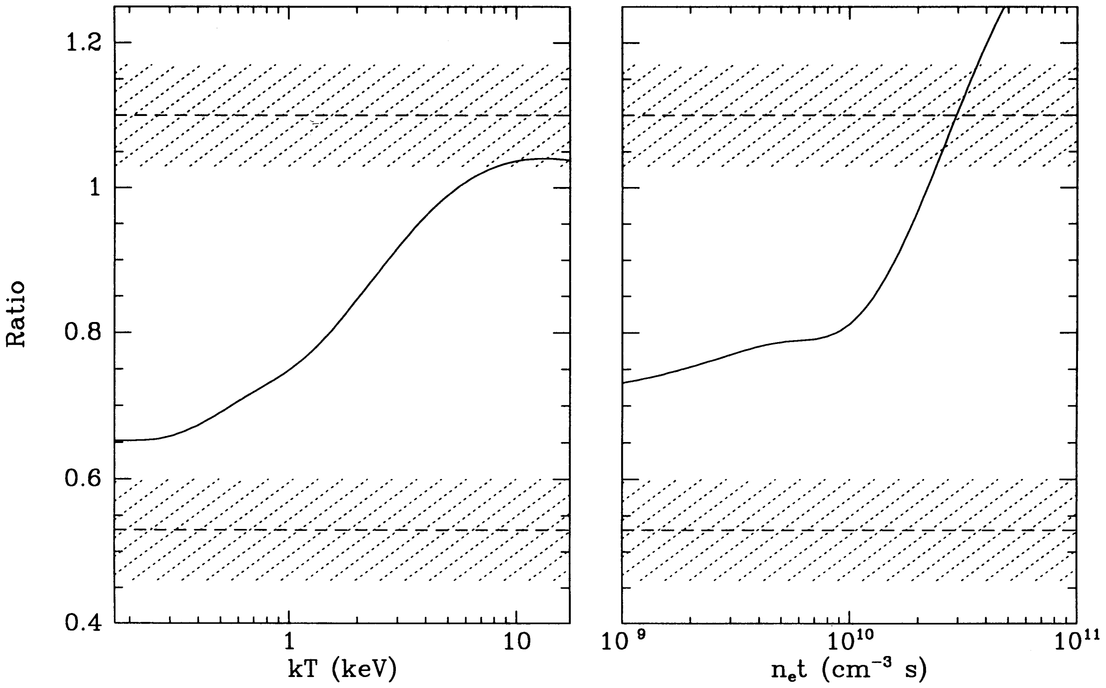

FIG. 9a FIG. 9b

FIG. 9.—Ionization timescale and temperature study. (*a*) Plotted is the predicted ratio image value as a function of plasma temperature kT with the ionization timescale fixed to the Tycho mean (log $n_e t = 10.04$), assuming complete mixing of the elemental ejecta. Extreme values (and 1 σ deviations) in the ratio image are denoted as cross-hatched regions. Notice that it is difficult to reproduce the entire range of ratio image values. (*b*) The predicted ratio image value as a function of $n_e t$ for a plasma with the temperature fixed at the mean ($kT = 1.72$ keV). It is difficult to reproduce the smallest observed values of the ratio image.

will be able to reproduce the low range of the Ratio image. In particular, for a ionization timescale an order of magnitude below the mean, the lowest ratio we can reproduce is 0.73.

We note that combined effects of kT and $n_e t$ variation may make it easier to reproduce the entire observed Ratio image range. Insofar as shocked ejecta with low kT (nearer the interior of the remnant) have been more recently shocked, simultaneous variations in kT and $n_e t$ may be an avenue for explaining some of the observed Ratio image. For conditions applicable to our study, we find that the transmission-corrected emissivity (Λ) of a plasma at high $n_e t$ or high kT is only a factor of 3 greater than that for a plasma with low values for these parameters. Thus, emission measure arguments do not rule out plasma effects with no abundance variation.

Nevertheless, the two knots of emission in the SE make a convincing argument for abundance variation. These two knots show markedly different hardness ratios. Yet, due to their similar size, proximity, and roughly equal distance from the remnant center, it is reasonable to believe that the two SE knots have similar temperature and ionization timescale diagnostics. We are thus guided to abundance variations as the source of their spectral dissimilarity.

In principle, we may further constrain ionization or temperature effects in Tycho by using the imaging results to generate a multi-kT or multi-$n_e t$ spectral model for comparison to the BBXRT data. For example we may fix the ionization timescale to the mean value and build-up a composite spectrum by assigning a unique value of kT to each occurrence of a particular value in the Ratio map. We can then compare, for example, the Si Lyα/Heα ratio in this composite spectrum to the actual BBXRT data for consistency. An upper limit on kT can be obtained from the upper limit of Si Lyα/Heα since the gas cannot be so hot as to have produced much hydrogen-like Si. Likewise the ionization timescale may be varied while the temperature is fixed. These studies are beyond the scope of our present work and will be deferred to a future paper. The origin of the variations in the Ratio map will only be answered definitively by an instrument such as *AXAF*, which will be capable of producing data with good spectral resolution and spatial resolution on the order of the features we see, or a few arcseconds.

4. CONCLUSION

We have used differencing between the *ROSAT* and *Einstein* HRI images of Tycho to obtain images representative of the 0.7–1.8 keV emission and 1.8–4.5 keV emission. We have found that the ratio of these two images contains regions whose values significantly deviate from the mean ratio. In particular, harder X-ray emission is found along much of the periphery, and there is evidence of softer emission from the interior and from the southern knot in the SE. It appears unlikely that variations in interstellar column density can reproduce the observed effects.

We believe that abundance effects are responsible for the variations in spectral hardness we observe, in which case there is at most incomplete mixing among the elemental constituents of the ejecta. Abundance variations in Si + S of at least 1.6 times the mean are required to reproduce spectrally hard regions in the data, while an Fe abundance of 2 times the mean is necessary for the soft regions. This interpretation is consistent with the morphology of emission we see in the *ROSAT*/*Einstein* imaging analysis and the abundances derived in non-equilibrium ionization BBXRT spectral fits in the context of ejecta models. Although in principle physical effects (such as differing kT or $n_e t$) may also be responsible for variations in spectral hardness across the remnant, it is difficult to reproduce the entire range of spectral hardness values seen. In particular, two spatially adjacent knots of emission in the SE show markedly different hardness ratios and are further evidence for elemental variation.

This research has made use of data obtained through the High Energy Astrophysics Science Archive Research Center Online Service, provided by the NASA–Goddard Space Flight Center. We wish to thank the staff at HEASARC for their support. This project was supported by NASA Astrophysics Data Program grant NAG5-1987 to the Smithsonian Astrophysical Observatory.

REFERENCES

Baade, W. 1945, ApJ, 96, 188
Becker, R. H., Holt, S. S., Smith, B. W., White, N. E., Boldt, E. A., Mushotzky, R. F., & Serlemitsos, P. J. 1979, ApJ, 234, L73
———. 1980, ApJ, 235, L5
Branch, D., Doggett, J. B., Nomoto, K., & Thielemann, F.-K. 1985, ApJ, 294, 619
Chevalier, R. A. 1982, ApJ, 258, 790
Chevalier, R. A., Blondin, J. M., & Emmering, R. T. 1992, ApJ, 392, 118
Chevalier, R. A., & Kirshner, R. P. 1979, ApJ, 233, 154
Chevalier, R. A., & Klein, R. I. 1978, ApJ, 219, 994
Cowie, L. L. 1975, MNRAS, 173, 429
de Korte, P. A. J., Bleeker, J. A. M., den Boggende, A. J. F., Branduardi-Raymont, G., Brinkmann, A. C., Culhane, J. L., Gronenschild, E. H. B. M., Mason, I., & McKechnie, S. P. 1981, Space Sci. Rev., 30, 495
Doggett, J. B., & Branch, D. 1985, AJ, 90, 2303
Fink, H. H., Asaoka, I., Brinkmann, W., Kawai, N., & Koyama, K. 1994, A&A, in press
Giacconi, R., et al. 1979, ApJ, 230, 540
Gull, S. F. 1973, MNRAS, 161, 47
Hamilton, A. J. S., Sarazin, C. L., & Szymkowiak, A. E. 1986, ApJ, 300, 713
Harris, D. E. 1984, *Einstein Observatory* Revised User's Manual
Henry, J. P., & Henriksen, M. J. 1986, ApJ, 301, 689
Hughes, J. P. 1991, in Supernovae, ed. S. E. Woosley (New York: Springer), 661
Hughes, J. P., & Helfand, D. J. 1984, ApJ, 291, 544
Hughes, J. P., & Singh, K. P. 1994, ApJ, 422, 126
Itoh, H., Masai, K., & Nomoto, K. 1988, ApJ, 334, 279
Jansen, F., Smith, A., Bleeker, J. A. M., de Korte, P. A. J., Peacock, A., & White, N. E. 1988, ApJ, 331, 949
Kamper, K., & van den Bergh, S. 1978, ApJ, 224, 851
Lucy, L. B. 1974, AJ, 79, 745
Morrison, R., & McCammon, D. 1983, ApJ, 270, 119
Nomoto, K., Thielemann, F.-K., & Yokoi, K. 1984, ApJ, 286, 644
Petre, R., et al. 1992, in Proc. COSPAR Symp., Recent Results in X-Ray and EUV Astronomy
Raymond, J. C. 1984, ARA&A, 22, 75
Raymond, J. C., & Smith, B. W. 1977, ApJS, 35, 419
Serlemitsos, P. J., et al. 1991, in Proc. 28th Yamada Meeting, Frontiers of X-Ray Astronomy, ed. Y. Tanaka & K. Koyama (Tokyo: Universal Academy), 221
Seward, F., Gorenstein, P., & Tucker, W. 1983, ApJ, 266, 287
Smith, A., Davelaar, J., Peacock, A., Taylor, B. G., Morini, M., & Robba, N. R. 1988, ApJ, 325, 288
Smith, R. C., Kirshner, R. P., Blair, W. P., & Winkler, P. F. 1991, ApJ, 375, 652
Taylor, B. G., Andresen, R. D., Peacock, A., & Zobl, R. 1981, Space Sci. Rev., 30, 479
Tsunemi, H., Yamashita, K., Masai, K., Hayakawa, S., & Koyama, K. 1986, ApJ, 306, 248
Woosley, S. E., Axelrod, T. S., & Weaver, T. A. 1984, in Stellar Nucleosynthesis, ed. C. Chiosi & A. Renzini (Dordrecht: Reidel), 263
Woosley, S. E., & Weaver, T. A. 1986, ARA&A, 24, 205
Zombeck, M. V., Conroy, M., Harnden, F. R. Jr., & Roy, A. 1990, in Proc. SPIE, Vol. 1344, EUV, X-Ray, and Gamma-Ray Instrumentation for Astronomy, 267